because it has nanoorder spatial resolution [9]. However, the scanning area in AFM is usually less than 10 μm. Therefore, AFM measurements are not suitable for observing the milliorder or microorder structure of cells and extracellular matrices; instead, these are usually observed at the single-cell or fiber level [10, 11]. Recently, the pipette aspiration technique [12], the ultrasonic detection technique [13, 14], and the scanning micro-indentation tester (SMIT) [15] have been used to measure the distribution of mechanical properties at the milli or microorder. AFM has not been used for a scanning measurement; instead, a one-point indentation test has been performed [16].

In our previous study we developed a scanning haptic microscopic (SHM) method for precise observation of the distribution of the elastic modulus over slices of natural tissue. The system is based on tactile sensor technology [17] that can measure the elastic modulus of living tissues from the cellular level [18] to the organ level [19]. SHM can precisely segregate elastin-rich and collagen-rich areas on the basis of the elastic modulus of aortic tissue [20]. Recently, we have revealed variations in the microscopic elastic structures along the entire length of the canine aorta and a correlation between the aortic elastic modulus and the elastin fiber content under no-load conditions [21].

In this study, we performed SHM measurements to observe variation of the microscopic elastic structures in canine thoracic aorta under static load conditions. The mechanical properties of collagen fibrils and elastic fibers, the two main extracellular matrices in vascular tissue, under physiological conditions were discussed.

Materials and methods

Preparation of aortic tissue samples

The animals used in this study received care in accordance with the Principles of Laboratory Animal Care (formulated by the National Institutes of Health, publication no.56-23, received 1985), and the research protocols (no. 12002) were approved by the ethics committee of the National Cardiovascular Center Research Institute.

Canine thoracic aortas ($n = 3$, located, ca 3 cm from the branch of the left subclavian artery; length ca 10 cm; inner diameter ca 6 mm) were obtained from beagle dogs (age ca 1 year; body weight ca 10 kg). Each aorta was divided into two segments (length ca 5 cm) and stored at −30 °C until measurement (ca 1 year). These arteries ($n = 6$) were then defrosted at room temperature and used for the measurements described below.

Scanning haptic microscope overview

Local elastic modulus images of cross sections of the aortas were obtained by use of an SHM (SHM-3000; P&M, Fukushima, Japan) at room temperature. Details of device configuration and principle of measurement have been reported elsewhere [17–21]. Briefly, the SHM system consists of a water bath, two stages, a microtactile sensor, two cameras, and a controller (Fig. 1a). The water bath is mounted along an XY-axis stage to enable horizontal movement when conducting measurements in a liquid environment. The microtactile sensor is mounted on a Z-axis stage to enable vertical movement. The two stages

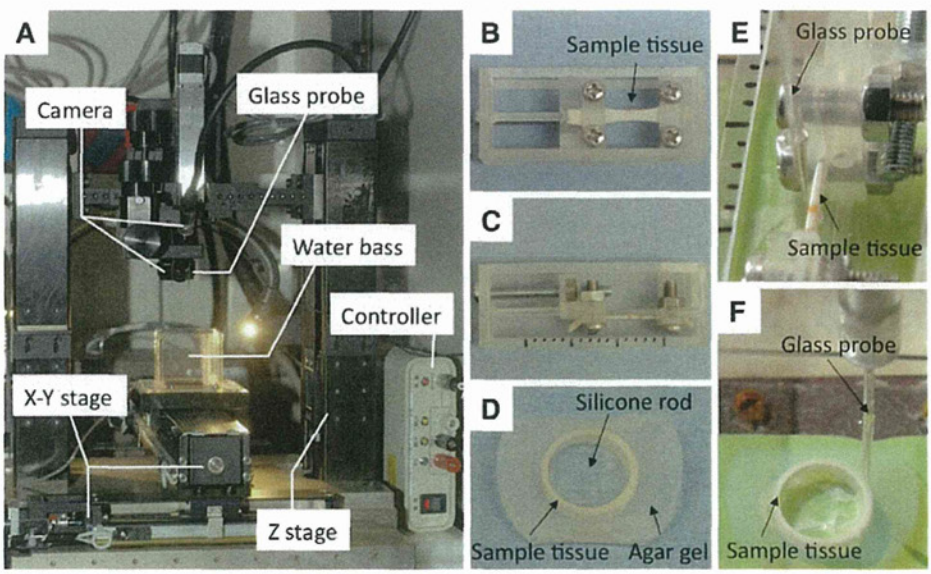

Fig. 1 **a** Photograph of scanning haptic microscope (SHM). *Front view* (**b**) and *top view* (**c**) of the sample holder in the tensile method, and *top view* (**d**) of sample with silicone rods embedded in agar gel in the rod-insertion method. SHM measurements were performed on the circumferential cross-sectional surface of the sample of aorta prepared by the tensile method (**e**) and the rod-insertion method (**f**)

with stepping motors are controlled by use of customized software running on a personal computer. One camera (WAT-231S2; Watec, Yamagata, Japan) is installed behind the sensor probe to enable observation of the entire sample area and setting of the measurement area. The other camera (CS9401-03; Toshiba Teli, Tokyo, Japan) is installed in front of the sensor probe to enable observation of the contact between the sensor tip and the sample surface. The sensor probe includes a glass needle and a lead zirconate titanate (PZT) sensor element. There are three electrodes in the PZT sensor element: input, output, and ground. The sensor unit operates on the basis of the phase-shift method [22]. The sensor probe is vibrated near the resonance frequency by applying an AC voltage to the PZT sensor element, and the vibration state is maintained by means of a phase shift circuit present in the controller as a feedback circuit for the vibration phase. The frequency is changed by contact between the sensor tip and the sample surface; this frequency change has an almost linear relationship with the elastic modulus of the sample [17]. The mapping of the pattern of the frequency change at each point across the entire measurement area of a sample was converted to an image of the distribution of the elastic modulus.

SHM measurement under two stretched conditions

Aortic tissue was stretched circumferentially by the tensile method or the rod-insertion method. In the former, the aorta was sliced into several rings (width 3 mm) that were cut open to obtain rectangular samples; these samples were then fixed on a sample holder that was specially designed by use of a 3D printer (Projet HD3000; 3D Systems, Rock Hill, SC, USA) to perform the tensile test (Fig. 1b, c). In the latter, the aorta was sliced into several rings (width 5 mm) into which silicone rods of different size were inserted; these rings were then completely embedded in 4 % agar gel (Nacalai Tesque, Kyoto, Japan) and cross-sectioned in the circumferential direction into slices ~3 mm thick by use of a microtome (VT1200S; Leica Microsystems Japan, Tokyo, Japan) to obtain disk-like portions with flat, embedded ring-like aorta samples (Fig. 1d). In both methods, the degree of stretching was set for specific strains of the aorta samples—0, 0.08, 0.15, 0.23, 0.38, and 0.80—corresponding to internal pressures of ca 0, 50, 100, 150, 250, and 600 mmHg, respectively, which were obtained by the luminal pressure–diameter relationship determined by use of the apparatus designed by Takamizawa and Hayashi [23].

The SHM measurement was performed in accordance with our previous report [20, 21]. Briefly, the sensor probe was previously calibrated with agar gels (concentration: 1–4 wt %, elastic modulus: 10–190 kPa), and the elastic modulus was examined by the force–deformation method by use of a 1-mm-diameter metal rod-indenter. The two stretched samples were fixed on the bottom of the water bath, and a saline solution was added until a specific height deemed appropriate for each probe was reached. The SHM measurement was conducted at room temperature on horizontal sections relative to the circumferential direction of the aortic tissue (Fig. 1e, f) without any preconditioning, in accordance with the previously reported method, in a point-by-point manner. The distance between two adjacent scanned points was 2 μm. The tip radius and indentation depth of the sensor probe were 5 and 10 μm, respectively. The overall scanning speed was approximately 3 points/s. The scanning area of each image was 160 × 80 μm (number of points, 3,200) at ~150 μm distance from the luminal surface.

Histological examination

After the SHM measurements, the stretched samples were fixed with 10 % formalin, embedded in paraffin, sliced into circumferential 4-μm-thick sections, and stained with elastica–van Gieson stain for elastin or sirius red stain for collagen. The orientation of the collagen was observed by obtaining polarizing microscope (Eclipse E1000; Nicon, Tokyo, Japan) images of the sirius red-stained samples.

Tensile test

Macroscopic tensile measurements of the aortic tissue were performed by use of a uniaxial tensile-testing apparatus (Rheoner II; Yamaden, Tokyo, Japan). Each sample was sliced into rings (width 3 mm), and the aortic ring was cut open to obtain rectangular strips. These strips were fixed in an upper and a lower grip (initial length ~10 mm), and a tensile load was applied in the circumferential direction by moving the lower grip at a rate of 0.05 mm/s until failure, i.e., tissue rupture.

Results

Scanning haptic microscope measurements for imaging the elastic modulus in saline solution at room temperature and optical microscopic observations after elastin or collagen staining were performed for samples of aorta stretched by means of the two methods, i.e. the tensile and rod-insertion methods (Fig. 2). In the distribution of the elastic modulus under no stretching, that is, no-strain conditions ($\varepsilon = 0$) corresponding to 0 mmHg, the stiff region consisted of elastin fibers that were stained deep purple by elastica–van Gieson stain, as demonstrated in our previous work [20, 21]. The soft region consisted of a mixture of collagen fibrils that were stained red by sirius red stain and smooth

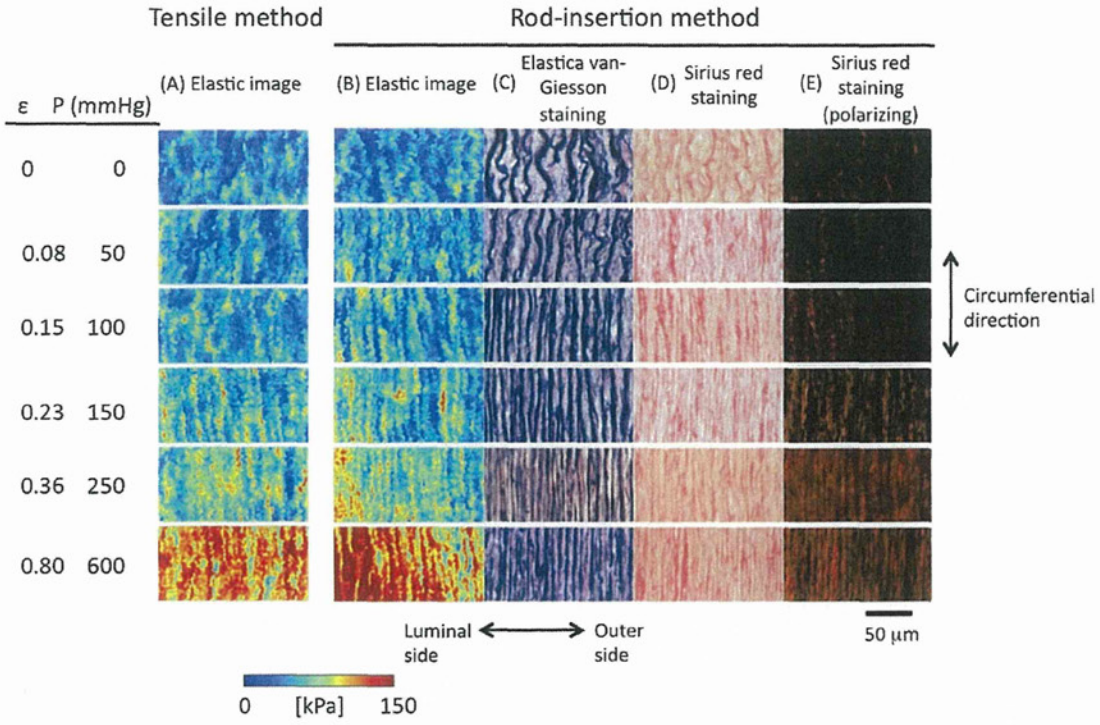

Fig. 2 Elastic images for the tensile method (**a**) and the rod-insertion method (**b**) obtained by SHM measurement (160 × 80 μm, 2-μm intervals). The *left-hand-side edge* of the elastic images is located ~150 μm from the luminal surface. The *color spectrum* indicates the elastic modulus (*red*, hard). Elastica–van Gieson (**c**) and sirius red staining (**d**) were performed after SHM measurements for the rod-insertion method. Specimens of sirius red staining were also observed by polarizing microscopy during observation of the orientation of collagen fibrils; the *brightness* indicates the degree of orientation of collagen (**e**)

muscle cells, neither of which could be segregated clearly by SHM on the basis of their different elastic modulus. On stretching in the circumferential direction by a physiological strain of 0.08–0.23 (50–150 mmHg), the wavy bundles with high elastic modulus almost straightened with an increase in the total elastic modulus (Fig. 3). There was little difference in the changing pattern between the two different stretching methods (Fig. 2a, b). A similar change pattern was observed for elastic fibers (Fig. 2c). A random pattern with a slight orientation was observed for collagen fibrils (Fig. 2d, e). Therefore, the stiff lines in the lamellar elastic modulus image composed of stiff and soft regions were caused by the stretched elastic fibers.

The total elastic modulus and high elastic modulus area both increased significantly over the physiological strain range ($\varepsilon > 0.36$, >250 mmHg), with few changes in the staining pattern of the collagen fibrils and thinning of the bundle of elastic fibers. On the other hand, highly circumferential orientation of the collagen fibrils was observed (Fig. 2e). At the highest strain ($\varepsilon = 0.80$, 600 mmHg) applied in this study, the regional elastic modulus was higher on the luminal surface side (133.6 kPa at $\varepsilon = 0.80$) than on the outer surface side (102.1 kPa) for the rod-insertion method (Fig. 2b), whereas it was similar for the luminal (111.2 kPa) and outer surface (108.4 kPa) sides for the tensile method.

Figure 3 shows the relationship between the strain and the averaged total elastic modulus of aorta stretched by the tensile and rod-insertion methods as determined by SHM measurement or by a traditional macroscopic tensile test. In both methods, the elastic modulus under a small strain increased almost linearly with the strain, and the slope of the increase was similar in both.

Discussion

As described above, the elastic image of aortic wall obtained by SHM was divided into stiff or soft regions under no-load conditions. The stiff region mainly comprises elastin fibers and the soft region mainly comprises collagen fibrils and smooth muscle cells [21]. The same result was obtained in this study (Fig. 2). Matsumoto et al. [15] performed microscopic measurement using SMIT under no-load conditions and reported that the high elastic modulus region of porcine thoracic aorta mainly comprised elastin. It is well known that collagen fibrils, which are hard structural proteins, are usually stiffer than elastin

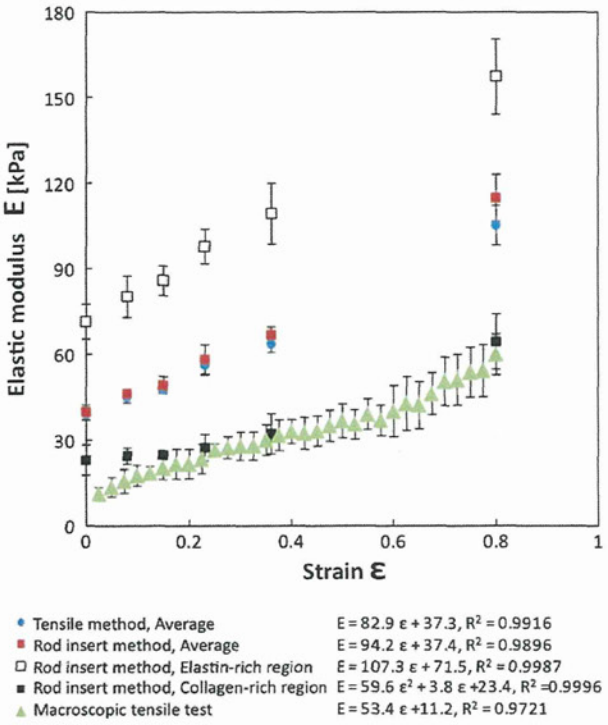

Fig. 3 Relationship between the strain and the elastic modulus as obtained by SHM measurements using the tensile and rod-insertion methods and the macroscopic tensile test. In both SHM measurements, the average elastic modulus was calculated for the total area (160 × 80 μm). Elastic moduli of elastin-rich and collagen-rich regions were calculated from those of stiffer and softer regions by the rod-insertion method (Fig. 2b). $N = 6$ (two samples were obtained from three dogs). The *error bar* shows the standard deviation

fibers, which are highly elastomeric [24]. In addition, in general, the mechanical behavior of soft tissues such as blood vessels is characterized by a "J"-shaped curve on a stress–strain diagram with a low-stiffness highly elastic zone giving rise to a high-stiffness zone. This behavior is attributed to the synergistic interplay of the two main structural proteins: elastin in the low-stiffness zone and collagen in the high-stiffness zone [3]. However, unfortunately, we could not clearly explain these contradictions in our previous SHM studies under no-load conditions. Therefore, the purpose of this study was to observe the change in the distribution of the local elastic modulus of aorta tissues under different strain conditions; this would help in clarifying the contribution of collagen to the mechanical property. A simple tensile method or pseudo-internal pressure loading method with rod-insertion could be used to directly map the elastic modulus distribution in the circumferential cross-sectional surface of the aorta using SHM for different strain conditions, including physiological pressure loading condition, although all conditions were under static strain.

In this study, under physiological conditions (50–150 mmHg), the highly elastic pattern (Fig. 2b) was similar to that in the elastin-stained photos (Fig. 2c). The average elastic modulus increased with elongation of the elastic fibers. At 150 mmHg, the elastic fiber was fully elongated and almost straightened. Therefore, the mechanical property of the aorta can be regarded as depending almost completely on the elastin fibers even under physiological conditions. Interestingly, there was no significant difference between the elastic modulus images obtained for the two different stretching methods up to 150 mmHg. Although these data were obtained from limited static methods, aortic tissues may be circumferentially stretched almost homogeneously in the wall from the luminal surface side to the outer side by pulsation in the body.

Collagen fibrils contributed little to the mechanical property even under physiological conditions. Collagen fibrils in vascular tissues may be lax in a natural, fully hydrated environment. On the other hand, above physiological conditions (>250 mmHg) they had a remarkable circumferential orientation (Fig. 2e) with a significant increase in the average elastic modulus (Fig. 2b), whereas there was little change in the collagen-fibril-stained photos (Fig. 2d). Although collagen fibrils are much stiffer than elastin fibers, they have little effect on the strength of the aorta under physiological conditions and contribute to the mechanical property mainly under high-load conditions. The burst pressure may be determined by the strength of the collagen fibrils. Therefore, the "J"-shaped curve obtained on a stress–strain diagram in the physiological pressure range may be attributable mainly to the elastic fibers and less to the collagen fibrils.

Two types of SHM measurement were performed in this study. One is the tensile method, which was performed to simulate aortic stretching conditions under a uniaxial tensile test. The other is the rod-insertion method, which was performed to simulate in vivo intravascular pressure. In both methods, the average elastic modulus was almost the same under each strain condition because the applied strain was almost the same. However, a difference between the elastic modulus of the luminal and outer sides was observed in the rod-insertion method in the high-pressure region, although little difference was observed in the tensile method. This might be attributable to the different strain between the luminal and outer sides. In the tensile method, the applied circumferential tensile strain was uniform on the arterial wall, but it was higher on the inner side than on the outer side in the rod-insertion method. This radial change in strain was also observed in vivo. Therefore, the rod-insertion method may be more suitable than the tensile method for arterial tissue. In addition, the tendency of the average elastic modulus to increase in both

SHM measurements was similar to that in the macroscopic tensile test, suggesting that the microscopic average feature is related to the macroscopic feature. These SHM measurements were believed to be appropriate for evaluating the mechanical property of arterial tissue under stretched conditions.

In this study, we proposed a mechanical measurement to compare the elastic structure of aortic tissue under different strain phases. The samples used in this measurement were frozen tissues. Therefore, the measured elastic modulus may differ from that of fresh tissues. However, a similar phenomenon was also observed for fresh tissues, and therefore, the frozen tissues were believed to be suitable model samples.

Many different conditions were found to have an effect on the elastic modulus under each strain phase. For example, the elastic modulus of bovine aorta wall decreased significantly from the inner to the outer side of the wall even under the no-load conditions [25]. Under pathological conditions, arteriosclerosis changes the morphology and mechanical properties of aortal walls [16]. It is noteworthy that the change in the micromechanical elastic properties of these samples can be observed with increasing strain. Furthermore, SHM measurements under different load conditions are expected to be helpful in the development and evaluation of artificial tissue.

Conclusion

We visualized the local elastic structure at the extracellular matrix level in canine aorta under different strain phases to reveal the variation in elastic properties. Strain was applied to aortic walls by two methods: the tensile method, which uniformly applies stress, and the rod-insertion method, which applies pseudo-internal pressure. The average elastic modulus in each strain phase was similar in both methods, and its tendency to increase was similar to that observed in the macroscopic tensile test. In the low or physiological strain phase (0–150 mmHg), the distribution of the elastic modulus was almost uniform in the radial direction in both methods. However, at higher strains (>250 mmHg), the distribution of the elastic modulus decreased from the inner to the outer side in the rod-insertion method, whereas it was almost uniform in the tensile method. It was inferred that the stress and/or strain of the aortic wall was almost uniform in the low and physiological strain phases, but that the stress followed a radial gradient at higher strain. The elastic modulus in stiff regions, which are mainly composed of elastin, increased linearly with the strain. In contrast, the elastic modulus in soft regions, which are mainly composed of collagen and smooth muscle cells, increased slightly in the low and physiological strain phases (0–150 mmHg) but the increase was greater at higher strains (>250 mmHg). We conclude that the pressure resistance of the aorta under physiological strain is mainly afforded by elastin; collagen fibrils contributed little except under much higher pressures.

Acknowledgments The authors thank Ms Manami Sone for her technical support in this study. This study was funded in part by a Grant-in-Aid for Scientific Research (B2465961, B23360374) from the Ministry of Education, Culture, Sports, Science and Technology of Japan.

References

1. Litwin SB, Cohen J, Fine S. Effects of sterilization and preservation on the rupture force and tensile strength of canine aortic tissue. J Surg Res. 1973;15:198–206.
2. Assoul N, Flaud P, Chaouat M, Letourneur D, Bataille I. Mechanical properties of rat thoracic and abdominal aortas. J Biomech. 2008;41:2227–36.
3. Angouras DC, Dosios TJ, Dimitriou CA, Chamogeorgakis TP, Rokkas CK, Manos TA, Sokolis DP. Surgical thoracic sympathectomy induces structural and biomechanical remodeling of the thoracic aorta in a porcine model. J Surg Res. 2012;172:68–76.
4. Wolinsky H, Glagov S. Structural basis for the static mechanical properties of the aortic media. Circ Res. 1964;14:400–13.
5. Hayashi K, Handa H, Nagasawa S, Okumura A, Moritake K. Stiffness and elastic behavior of human intracranial and extracranial arteries. J Biomech. 1980;13:175–84.
6. Dobrin PB, Rovick AA. Influence of vascular smooth muscle on contractile mechanics and elasticity of arteries. Am J Physiol. 1969;217:1644–51.
7. Vaishnav RN, Young JT, Patel DJ. Distribution of stresses and of strain-energy density through the wall thickness in a canine aortic segment. Circ Res. 1973;32:577–83.
8. Matsumoto T, Hayashi K. Stress and strain distribution in hypertensive and normotensive rat aorta considering residual strain. J Biomech Eng. 1996;118:62–73.
9. Binnig G, Quate CF, Gerber C. Atomic force microscope. Phys Rev Lett. 1986;56:930–3.
10. Zhang Y, Hu X, Sun J, Shen Y, Hu J, Xu X, Shao Z. High-resolution imaging and nano-manipulation of biological structures on surface. Microsc Res Tech. 2011;74:614–26.
11. Yang L, van der Werf KO, Koopman BF, Subramaniam V, Bennink ML, Dijkstra PJ, Feijen J. Micromechanical bending of single collagen fibrils using atomic force microscopy. J Biomed Mater Res A. 2007;82:160–8.
12. Ohashi T, Kato Y, Matsumoto T, Sato M. Intramural distribution of elastic moduli in thoracic aortas and its relationship to histology: comparison between porcine and bovine thoracic aortas. JSME Int J Ser C. 1999;42:568–73.
13. Kanai H, Hasegawa H, Ichiki M, Tezuka F, Koiwa Y. Elasticity imaging of atheroma with transcutaneous ultrasound: preliminary study. Circulation. 2003;107:3018–21.
14. Kim K, Jeong CG, Hollister SJ. Non-invasive monitoring of tissue scaffold degradation using ultrasound elasticity imaging. Acta Biomater. 2008;4:783–90.
15. Matsumoto T, Goto T, Furukawa T, Sato M. Residual stress and strain in the lamellar unit of the porcine aorta: experiment and analysis. J Biomech. 2004;37:807–15.
16. Tracqui P, Broisat A, Toczek J, Mesnier N, Ohayon J, Riou L. Mapping elasticity moduli of atherosclerotic plaque in situ via atomic force microscopy. J Struct Biol. 2011;174:115–23.

17. Murayama Y, Omata S. Fabrication of micro tactile sensor for the measurement of micro-scale local elasticity. Sens Actuators A. 2004;109:202–7.
18. Murayama Y, Constantinou CE, Omata S. Micro-mechanical sensing platform for the characterization of the elastic properties of the ovum via uniaxial measurement. J Biomech. 2004;37:67–72.
19. Murayama Y, Constantinou CE, Omata S. Development of tactile mapping system for the stiffness characterization of tissue slice using novel tactile sensing technology. Sens Actuators A. 2005;120:543–9.
20. Oie T, Suzuki H, Murayama Y, Fukuda T, Omata S, Kanda K, Takamizawa K, Nakayama Y. Surface elasticity imaging of vascular tissues in a liquid environment by a scanning haptic microscope. J Artif Organs. 2010;13:121–5.
21. Moriwaki T, Oie T, Takamizawa K, Murayama Y, Fukuda T, Omata S, Kanda K, Nakayama Y. Variations in local elastic modulus along the length of the aorta as observed by use of a scanning haptic microscope (SHM). J Artif Organs. 2011; 14:276–83.
22. Omata S, Terunuma Y. New tactile sensor like the human hand and its application. Sens Actuators A. 1992;35:9–15.
23. Takamizawa K, Hayashi K. Strain energy density function and uniform strain hypothesis for arterial mechanics. J Biomech. 1987;20:7–17.
24. Gosline J, Lillie M, Carrington E, Guerette P, Ortlepp C, Savage K. Elastic proteins: biological roles and mechanical properties. Philos Trans R Soc Lond B Biol Sci. 2002;357:121–32.
25. Matsumoto T, Sato M. Analysis of stress and strain distribution in the artery wall consisted of layers with different elastic modulus and opening angle. JSME Int J Ser C. 2002;45:906–12.

JOURNAL OF
Medical
Engineering
&Technology

http://informahealthcare.com/met
ISSN: 0309-1902 (print), 1464-522X (electronic)

J Med Eng Technol, 2013; 37(2): 96–101
 DOI: 10.3109/03091902.2012.747008

informa
healthcare

INNOVATION

Surface density mapping of natural tissue by a scanning haptic microscope (SHM)

Takeshi Moriwaki[1,2], Tomonori Oie[1,3], Keiichi Takamizawa[1], Yoshinobu Murayama[4], Toru Fukuda[4], Sadao Omata[4], and Yasuhide Nakayama*[1,2]

[1]*Division of Medical Engineering and Materials, National Cerebral and Cardiovascular Center Research Institute, Fujishiro-dai, Osaka, Japan,* [2]*Cell Engineering Unit, Graduate School of Chemical Science and Engineering, Hokkaido University, Kita-ku, Sapporo, Japan,* [3]*Shinkan Kogyo Co. Takeshima, Nishiyodogawa-ku, Osaka, Japan, and* [4]*NEWCAT Institute, College of Engineering, Nihon University, Nakagawara, Tokusada, Tamura, Koriyama, Fukushima, Japan*

Abstract

To expand the performance capacity of the scanning haptic microscope (SHM) beyond surface mapping microscopy of elastic modulus or topography, surface density mapping of a natural tissue was performed by applying a measurement theory of SHM, in which a frequency change occurs upon contact of the sample surface with the SHM sensor – a microtactile sensor (MTS) that vibrates at a pre-determined constant oscillation frequency. This change was mainly stiffness-dependent at a low oscillation frequency and density-dependent at a high oscillation frequency. Two paragon examples with extremely different densities but similar macroscopic elastic moduli in the range of natural soft tissues were selected: one was agar hydrogels and the other silicon organogels with extremely low (less than 25 mg/cm^3) and high densities (ca. 1300 mg/cm^3), respectively. Measurements were performed in saline solution near the second-order resonance frequency, which led to the elastic modulus, and near the third-order resonance frequency. There was little difference in the frequency changes between the two resonance frequencies in agar gels. In contrast, in silicone gels, a large frequency change by MTS contact was observed near the third-order resonance frequency, indicating that the frequency change near the third-order resonance frequency reflected changes in both density and elastic modulus. Therefore, a density image of the canine aortic wall was subsequently obtained by subtracting the image observed near the second-order resonance frequency from that near the third-order resonance frequency. The elastin-rich region had a higher density than the collagen-rich region.

Keywords

Density, imaging, mapping, microscope, tissue

History

Received 14 September 2012
Revised 31 October 2012
Accepted 1 November 2012

1. Introduction

Examining the physical properties of natural tissues is essential for evaluating biological functions. In addition, to localize the sites of disease, various physical or mechanical measurements from basic to clinical are performed. The elastic modulus, which is one of the most well-known physical properties, has been widely measured by tensile [1–3] and pressure load tests [4,5]. In microscopic tests, an atomic force microscope is used to observe the elastic structure of a cell or extracellular matrix [6–8]. Like the elastic modulus, density is a basic physical property directly related to the strength of tissues. A density test is primarily performed to evaluate the strength of bone [9,10]. In addition, ultrasonography is used for detecting the area of a tumour [11,12]. Given that ultrasonic measurements are non-invasive, many studies have been performed to reveal acoustic properties that are closely related to the elastic modulus and density of tissues [13–16]. Although the usability and spatial resolution of ultrasonic imaging have increased every year, the next step of improving its quantitative capability is a serious problem.

In a previous study, we developed a scanning haptic microscope (SHM) to precisely observe the mapping of elastic modulus or topography over slices of natural tissue samples. The SHM, which is based on resonance-based contact impedance measurement [17] and the phase-shift method [18], detects changes in the frequency of contacts between the sample surface and tip of a microtactile sensor (MTS) probe [19]. The SHM can precisely segregate elastin- and collagen-rich areas based on the elastic modulus of aortic tissues [20]. We have revealed variations in the microscopic elastic structures along the entire length of the canine aorta [21].

In this study, to expand the performance capacity of the SHM beyond the above-mentioned microscopic surface mapping of elastic modulus or topography, we performed

*Corresponding author. Email: nakayama@ri.ncvc.go.jp

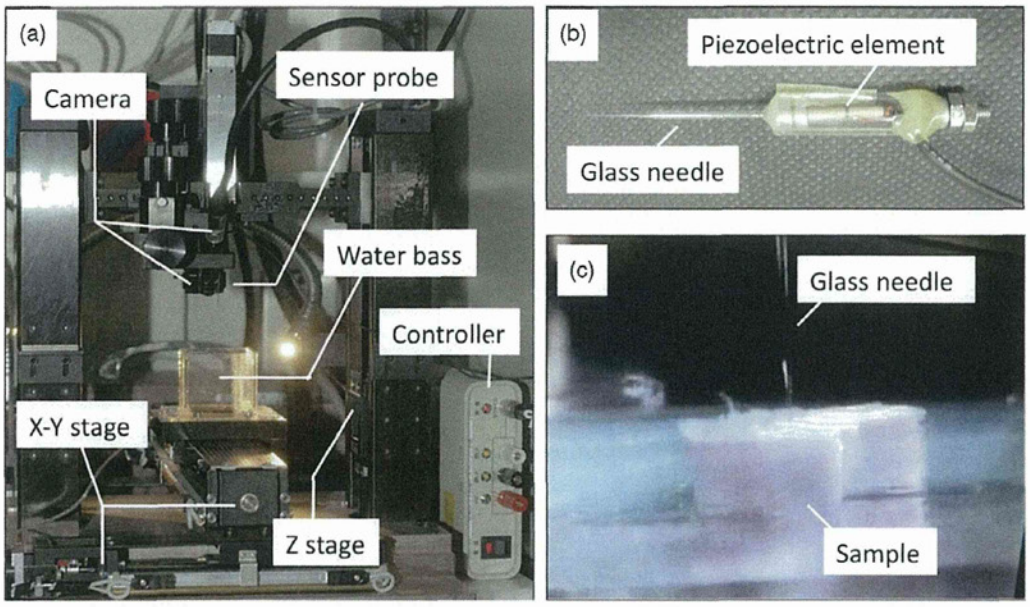

Figure 1. Photographs of scanning haptic microscope (a) and microtactile sensor probe (b). A change in frequency occurs by contact between sensor probe and sample surface (c).

surface density mapping of a natural tissue by applying a working theory of SHM measurement. After evaluating the possibility of density measurement with the SHM by using two paragon examples with extremely different densities of low-density agar hydrogels and high-density silicone organogels, we performed density mapping by using canine artery tissue.

2. Materials and methods

2.1. Materials

Agar hydrogels, silicone organogels and canine aorta were used as the samples. Four kinds of agar hydrogels – 10, 15, 20 or 25 mg cm^{-3} in density with a corresponding elastic modulus of 19, 60, 108 or 170 kPa – were prepared by heating an aqueous solution of agar (Nacalai Tesque, Kyoto, Japan; concentration of 1.0, 1.5, 2.0 or 2.5 wt/v%, respectively) and then letting it stand at room temperature. Four kinds of silicone organogels with the same density of ~1300 mg cm^{-3} but different elastic modulus (13, 48, 104 or 201 kPa) were obtained from Shin-Etsu Chemical Co. (KE-116, Tokyo, Japan). After approval by the research ethics committee at the National Cerebral and Cardiovascular Center (Application No. 12010), the aortic arch length, ~5 cm; inner diameter, ~8 mm) was harvested from a beagle (age, ~1 year; body weight, ~10 kg) and stored at −30 °C. The aortic samples ($n = 10$) were prepared by embedding the aorta in 4 wt/v% agar in the no-load state and cutting it into horizontally circumferential slices 1 mm thick by using a microtome (VT1200S; Leica Microsystems Japan, Tokyo, Japan).

2.2. Measurement of macroscopic elastic modulus

The macroscopic elastic modulus of agar hydrogels or silicone organogels was measured by the traditional force-deformation method with a 1-mm-diameter metal rod-indenter [17,22]. The indentation speed was 3.3 μm s^{-1}. The range of the indentation depth, which was used to calculate the elastic modulus, was 10–50 μm.

2.3. Scanning haptic microscope (SHM) observations

The elastic modulus [20,21], topography [20,21] or density was imaged by SHM (SHM-3000, P&M Co., Fukushima, Japan, Figure 1a). The SHM is equipped with three stepping motor stages of sub-micrometre resolution and a sensor probe of sub-micrometre resolution to precisely scan and approach the sample. The sensor includes a glass needle and a lead zirconate titanate (PZT) sensor element with input, output and ground electrodes (Figure 1b). The sample was fixed to the bottom of the water bath in the SHM (Figure 1c) and a saline solution was added to the bath up to an appropriate depth, determined for each MTS according to our previous report [20].

The frequency change generated at the contact between the MTS sensor and the two types of samples (agar hydrogels and silicone organogels) was measured using 10 sensor probes at two frequencies near the second-order (177–210 kHz) and third-order (225–295 kHz) resonance frequencies based on the characteristic of each MTS. These measurements were performed at 100 points in a point-by-point manner in accordance with our previous report [21]. The distance between two adjacent scanned points was 10 μm (scanning area, 100 × 100 μm). Results are expressed as mean ± standard deviation of the mean. The tip diameter and indentation depth of MTS were 5 and 10 μm, respectively. The overall scanning speed was ~3 points s^{-1}.

The surface topography mapping of an aortic sample was obtained from the height of the MTS at the contact with the sample at each point. The mapping of the pattern of frequency change at each point across the entire measurement area of the

J Med Eng Technol, 2013; 37(2): 96–101

aortic sample by using the above-mentioned frequencies near the second-order resonance frequency of the MTS showed a distribution of the relative elastic modulus of the sample. The relative density image of an aortic sample was obtained by mapping the difference between the frequency change data obtained by scanning the sample surface (area: 150 × 150 μm) near the second-order resonance frequency of the MTS and that near the above-mentioned third-order resonance frequency. The distance between two adjacent scanned points was 2 μm (total number of points: 5625).

2.4. Principle of surface density mapping by SHM

The SHM was developed for mapping the surface microscopic elastic modulus simultaneously with the topography of natural tissues at scan sizes ranging from the cellular to organic levels. Elastic modulus measurement in the SHM is based on changes in the oscillation frequency of the sensor probe induced by the contact impedance (Z) generated upon its contact with the sample surface. The vertical vibration induced by Z in a rigid circular disk on a semi-infinite elastic solid has been solved in several studies [17,23–25] and is adequately expressed by the equation in Figure 2. In this equation, r_x, m_x, k_x and ω denote the equivalent radiation resistance, mass, stiffness and angular velocity (i.e. the oscillation frequency), respectively. The coefficients a_{21} and a_{11} are functions of Poisson's ratio, whose numerical values were reported by Gladwell and Kleesattel [23]. The value of r_x is independent of the oscillation frequency. In contrast, the values for ωm_x and k_x/ω increase and decrease, respectively, as the oscillation frequency increases. Therefore, when the contact area, S, and oscillation frequency, ω, are sufficiently small, k_x/ω dominates Z and the frequency change at the contact well reflects the elastic modulus of the sample, E_x. Conversely, when the contact area and oscillation frequency are sufficiently large, ωm_x dominates Z and the frequency change at the contact well reflects the density of sample, ρ_x. When S is constant, the frequency change is mainly stiffness-dependent at a low oscillation frequency and mainly density-dependent at a high oscillation frequency. Therefore, the SHM is considered to be capable of evaluating the microscopic density of the sample surface by changing the oscillation frequency at the measurement site.

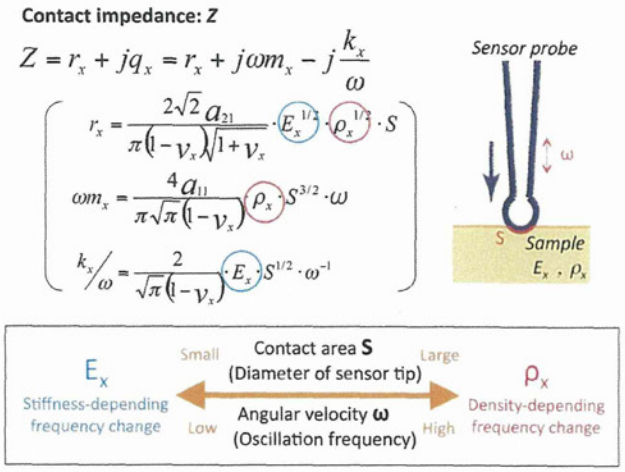

Figure 2. Theoretical equation for calculating contact impedance, Z. Here, r_x, m_x and k_x denote the equivalent radiation resistance, mass and stiffness, respectively. ν_x, E_x, ρ_x, S and ω are the Poisson ratio, elastic modulus, density, contact area and angular velocity, respectively. The coefficients a_{21} and a_{11} are functions of Poisson's ratio, whose numerical values were reported by Gladwell and Klesattel [23]. According to these equations, when the tip diameter and oscillation frequency are sufficiently small, k_x/ω dominates the contact impedance, and the frequency change at the contact well reflects the elastic modulus of the sample. Conversely, when the tip diameter and oscillation frequency are sufficiently large, ωm_x dominates the contact impedance and the frequency change at the contact well reflects the sample density.

3. Results

3.1. Dependency of frequency changes on density

To examine the possibility of density measurement by SHM, two types of samples with extremely different density were selected: agar hydrogels, which were fully swollen in water and had extremely low densities of less than 25 mg cm^{-3}; and silicone organogels, which had no water content and an extremely high density of ~1300 mg cm^{-3}. For each type of sample, four kinds with different macroscopic elastic moduli ranging from ~10–200 kPa were prepared.

Typical frequency changes of the MTS, generated by contact between the tip of the MTS and the sample surface at the two different frequencies near the second- and third-order resonance frequencies on all gels, were plotted against their corresponding macroscopic elastic moduli obtained by the traditional force-deformation method (Figure 3). Nearly linear relationships were obtained at both resonance frequencies for the two types of gels. There was little difference in the slopes of the agar and silicone samples, which were ~0.018 and 0.016, respectively. On the other hand, in the silicone samples, a large difference was observed between the intercepts of the two linear relationships obtained from measurements near the second- and third-order resonance frequencies, whereas almost the same intercepts were observed in the agar samples. The average difference of the intercept between the two resonance frequencies in 10 sensor probes was 0.06 ± 0.14 for agar samples and 0.60 ± 0.24 for silicone samples (Figure 3b).

3.2. Density mapping of artery

SHM measurements were performed on aortic samples near the second- and third-order resonance frequencies (Figure 4). In the topographical images, the surface profiles of the samples differed little between measurements near the second- (Figure 4a) and third-order (Figure 4b) resonance frequencies. On the other hand, the frequency change obtained near the third-order resonance frequency (Figure 4d) was higher than that near the second-order resonance frequency (Figure 4c), which was related mainly to the elastic modulus. The relative density image (Figure 4e) was obtained by subtracting the frequency change data near the second-order resonance frequency from those near the third-order resonance frequency.

4. Discussion

In this study, semi-quantitative measurement of the surface density by an SHM was successfully achieved as a frequency

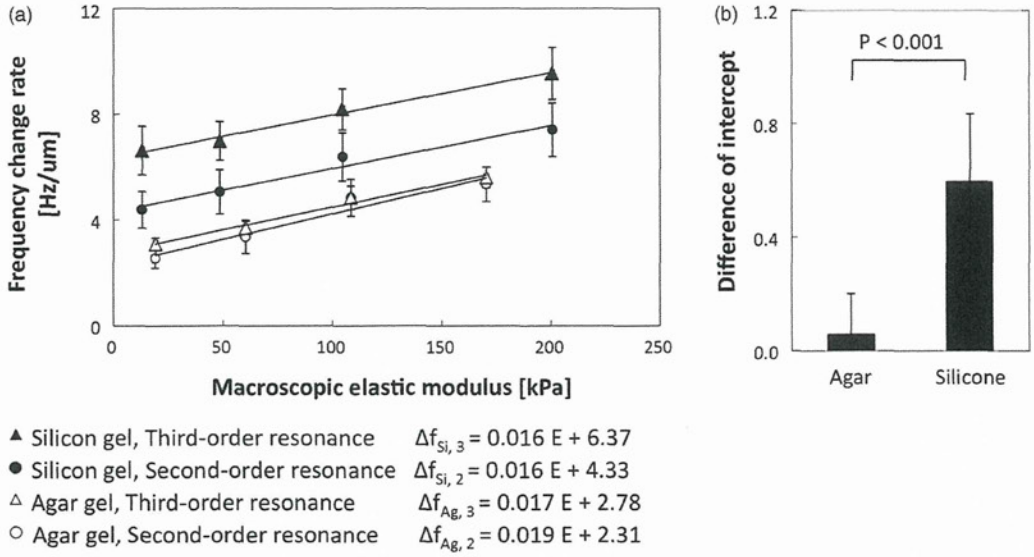

Figure 3. (a) Relationships between frequency change rates measured by the scanning haptic microscope (SHM) and macroscopic elastic moduli measured by force deformation method. Agar hydrogels and silicone organogels were measured by the SHM near second- (177 kHz) and third-order (225 kHz) resonance frequencies. Frequency change rate near third-order resonance frequency is corrected so as to equal frequency change rates between second- and third-order resonance frequencies for 2.0 wt% agar gel (multiplied by ratio of frequency change rates measured near second- and third-order resonance frequencies), in order to match detection sensitivities of frequency changes of both measurement parameters. (b) Difference of intercept between linear relationships near second- and third-order resonance frequencies (samples, agar hydrogels and silicone organogels; number of probes, 10). To standardize detection sensitivity of frequency change between sensor probes, intercepts of each sensor are divided by frequency change rate values of each sensor for 2.0 wt% agar gel.

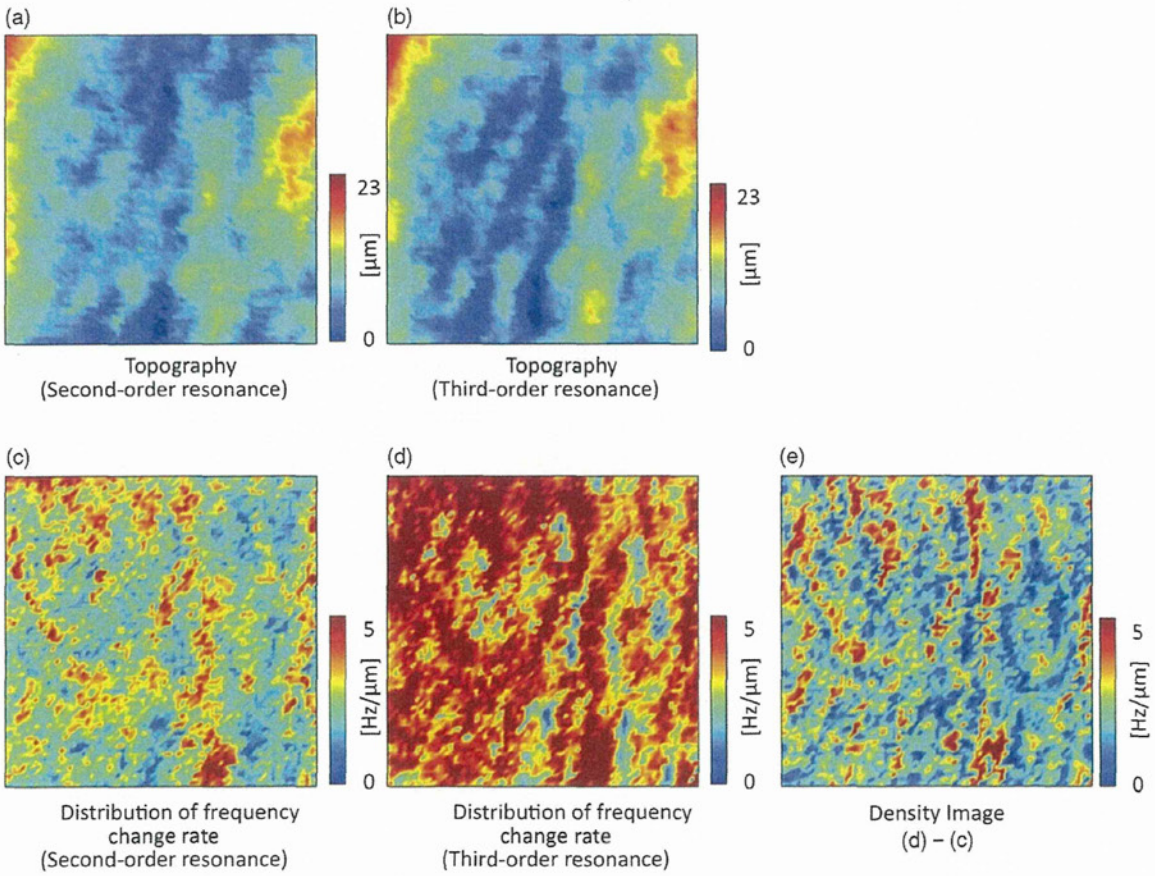

Figure 4. Topography (a, b) and map of frequency change rate (c, d) measured by the SHM near second- and third-order resonance frequencies (measurement area: 150 × 150 µm). Values of frequency change rate in (d) are corrected by similar method in Figure 3 to match detection sensitivities between second- and third-order resonance frequencies. Difference map of frequency change rate between second- and third-order resonance frequencies (e) adequately reflect density distribution of measurement area, according to theory of contact impedance and results in Figure 3.

change by using two types of gel samples and mapping of this surface density was clearly demonstrated in an aortic sample. Surface density mapping is a novel function of the SHM in addition to the previously achieved mappings of surface elastic modulus and topography. Furthermore, this is the first report of microscopic observations of the developed mapping. Two paragon gels of extremely different density were selected as samples: agar hydrogels of extremely low density (less than $25\,mg\,cm^{-3}$) and silicone organogels of extremely high density ($\sim 1300\,mg\,cm^{-3}$). In calculating the density, the water content was excluded because SHM measurements were performed in normal saline to avoid the drying of samples and to simulate *in vivo* conditions. The macroscopic elastic modulus of the agar gels, measured by the traditional force-deformation method, could be controlled by their preparation concentrations and the elastic modulus of the silicone gels could be controlled by the amount of cross-linkers. The macroscopic elastic modulus of all gels could be easily adjusted to that of soft natural tissues, which ranges from ~10–200 kPa. Therefore, the two types of samples were appropriate for this study.

In both gels, the frequency changes increased nearly linearly with an increase in the macroscopic elastic modulus in the measurements near the second-order resonance frequency (Figure 3). The amount of frequency change corresponded to the magnitude of microscopic elastic modulus, as reported in our previous papers. On the other hand, in the measurements near the third-order resonance frequency, a nearly identical linear relationship between the macroscopic modulus and frequency change rate was obtained for the low-density agar gels, whereas the relationship shifted to higher frequency change rates for the high-density silicone gels. This shift was independent of the macroscopic elastic modulus. As explained above, in the measurements at the higher resonance frequency, the influence of density increased. Other elements restricting the vibration of the MTS were negligible in these measurements. Therefore, the density could be expressed as a difference between the frequency change rates near the second- and third-order resonance frequencies, i.e. the difference between the intercepts of the two relationships, across the entire macroscopic elastic range of soft natural tissues.

In this study, two kinds of samples with extremely different densities were used. In the next step, hydrogels with densities controlled in a stepwise manner in an elastic modulus range similar to that of soft natural tissues will be used. After calibration, further quantitative density mapping will be obtained by SHM measurement. For example, acid-soluble collagen gels may be suitable for calibration because their elastic moduli may vary with the pH at gelation under the same concentration (density) [26,27]. In addition, in theory, the measured frequency change of the MTS mainly reflects the elastic modulus of the sample by using an MTS with a tip diameter of less than 1 μm, whereas it mainly reflects the density of the sample by using an MTS with a tip diameter of more than 50 μm, albeit with poor spatial resolution. Furthermore, improving the measurement sequence will achieve more accurate density imaging. In this study, SHM observations near the third-order resonance frequency were performed after those near the second-order resonance frequency. If the two frequency measurements were alternated at each measurement point, the spatial gap between the two obtained images will be negligible.

As reported in our previous study [20], measurement of aortic samples near the second-order oscillation frequency revealed a lamellar structure with stiff and soft regions, which were composed of elastin fibres and collagen fibrils with smooth muscle cells, respectively (Figure 4c). In Figure 4(e), a similar lamellar structure was observed, indicating that the elastin-rich and collagen-rich regions had high and low densities, respectively. Ng et al. [28] and Conde et al. [29] reported that elastin and collagen contents in the arterial wall of rats were ~60% and 30%, respectively, by histological analysis. On the other hand, Debrah et al. [30] reported that the collagen-to-total protein ratio was less than 20% in the arterial wall of mice and Tran et al. [31] reported that the amount of collagen was over 100-times less than that of elastin in the arterial wall of humans by mass analysis using enzymes. These results support our results that the density of the collagen-rich region in the arterial wall was lower than that of the elastin-rich region. That collagen fibrils are far stiffer than elastin fibres is well known [32]. However, collagen fibrils are sparse and assume a fully hydrated state in the arterial wall, especially under a no-load condition. Although individual elastin fibres may be softer than collagen fibrils, a thick band of elastin fibres is stiffer than a sparse collagen-rich region; additionally, elastin-rich regions were measured to be stiffer and higher in density than collagen-rich regions in the present SHM measurements.

Density imaging, which has micro-level spatial resolution, enables evaluation of the density of individual extracellular matrices. In developing tissue-engineered artificial tissues in particular, density imaging is useful in suggesting design guidelines and evaluating the quality of fractures. Additionally, that tumours undergo changes in elastic modulus and density is well known; hence, simultaneous measurement of these changes by SHM may be useful for the early detection of tumours.

In conclusion, surface density mapping was first demonstrated as a function to extend the performance of an SHM. The SHM was thus endowed with the three functions of mapping the density, elastic modulus and topography of the surface on sliced natural soft tissues. In future studies, quantitative measurements will be obtained after calibration with specially designed samples. In addition, as the performance capacity of the SHM is further expanded to measuring the binding force (e.g. adhesive or electrostatic force) induced by contact of the MTS tip with the sample surface, the SHM will likely be developed into multi-performance microscopic imaging device.

Acknowledgements

The authors thank P&M Co. for providing the SHM-3000 and Mr T. Yamaguchi for technical support in SHM measurement. This study was funded in part by Grants-in-Aid for Scientific Research (B24360162, B23360374) from the Ministry of Education, Culture, Sports, Science, and Technology of Japan.

Declaration of interest

The authors report no conflicts of interest. The authors alone are responsible for the content and writing of this article.

References

1. Angouras, D.C., Dosios, T.J., Dimitriou, C.A., Chamogeorgakis, T.P., Rokkas, C.K., Manos, T.A., and Sokolis, D.P., 2012, Surgical thoracic sympathectomy induces structural and biomechanical remodeling of the thoracic aorta in a porcine model. *Journal of Surgical Research*, **172**, 68–76.
2. Assoul, N., Flaud, P., Chaouat, M., Letourneur, D., and Bataille, I., 2008, Mechanical properties of rat thoracic and abdominal aortas. *Journal of Biomechanics*, **41**, 2227–2236.
3. Lake, S.P., Miller, K.S., Elliott, D.M., and Soslowsky, L.J., 2010, Tensile properties and fiber alignment of human supraspinatus tendon in the transverse direction demonstrate inhomogeneity, nonlinearity, and regional isotropy. *Journal of Biomechanics*, **43**, 727–732.
4. Wolinsky, H., and Glagov, S., 1964, Structural basis for the static mechanical properties of the aortic media. *Circulation Research*, **14**, 400–413.
5. Hayashi, K., Handa, H., Nagasawa, S., Okumura, A., and Moritake, K., 1980, Stiffness and elastic behavior of human intracranial and extracranial arteries. *Journal of Biomechanics*, **13**, 175–184.
6. Zhang, Y., Hu, X., Sun, J., Shen, Y., Hu, J., Xu, X., and Shao, Z., 2011, High-resolution imaging and nano-manipulation of biological structures on surface. *Microscopy Research Technique*, **74**, 614–626.
7. Yang, L., van der Werf, K.O., Koopman, B.F., Subramaniam, V., Bennink, M.L., Dijkstra, P.J., and Feijen, J., 2007, Micromechanical bending of single collagen fibrils using atomic force microscopy. *Journal of Biomedical Materials Research Part A*, **82**, 160–168.
8. Raman, A., Triqueros, S., Cartagena, A., Stevenson, A.P., Susilo, M., Nauman, E., and Contera, S.A., 2011, Mapping nanomechanical properties of live cells using multi-harmonic atomic force microscopy. *Nature Nanotechnology*, **6**, 809–814.
9. Chun, K.J., 2011, Bone densitometry. *Seminars in Nuclear Medicine*, **41**, 220–228.
10. Kinds, M.B., Bartels, L.W., Marijnissen, A.C., Vincken, K.L., Viergever, M.A., Lafeber, F.P., and de Jong, H.W., 2011, Feasibility of bone density evaluation using plain digital radiography. *Osteoarthritis Cartilage*, **19**, 1343–1348.
11. Aoki, T., Moriyasu, F., Yamamoto, K., Shimizu, M., Yamada, M., and Imai, Y., 2011, Image of tumor metastasis and inflammatory lymph node enlargement by contrast-enhanced ultrasonography. *World Journal of Radiology*, **3**, 298–305.
12. Gomez, N.R., Kouniavsky, G., Tsai, H.L., Somervell, H., Pai, S.I., Tufano, R.P., Umbricht, C., Kowalski, J., Dackiw, A.P., and Zeiger, M.A., 2011, Tumor size and presence of calcifications on ultrasonography are pre-operative predictors of lymph node metastases in patients with papillary thyroid cancer. *Journal of Surgical Oncology*, **104**, 613–616.
13. Hachiya, H., Ohtsuki, S., and Tanaka, M., 1994, Relationship between speed of sound in and density of normal and diseased rat livers. *Japanese Journal of Applied Physics*, **33**, 3130–3133.
14. Yamaguchi, T., and Hachiya, H., 2010, Proposal of parametric imaging method for quantitative diagnosis of liver fibrosis. *Journal of Medical Ultrasonics*, **37**, 155–166.
15. Ikeshita, K., Hasegawa, H., and Kanai, H., 2012, Improvement in accuracy of ultrasonic measurement of transient change in viscoelasticity of radial arterial wall due to flow-mediated dilation by adaptive low-pass filtering. *Japanese Journal of Applied Physics*, **51**, 07GF14:1–7.
16. Saijo, Y., 2009, Acoustic microscopy: Latest developments and applications. *Imaging in Medicine*, **1**, 47–63.
17. Kleesattel, C., and Gladwell, G.M.L., 1968, The contact–impedance meter-1. *Ultrasonics*, **6**, 175–180.
18. Omata, S., and Terunuma, Y., 1992, New tactile sensor like the human hand and its application. *Sensors and Actuators A*, **35**, 9–15.
19. Murayama, Y., and Omata, S., 2004, Fabrication of micro tactile sensor for the measurement of micro-scale local elasticity. *Sensors and Actuators A*, **109**, 202–207.
20. Oie, T., Suzuki, H., Murayama, Y., Fukuda, T., Omata, S., Kanda, K., Takamizawa, K., and Nakayama, Y., 2010, Surface elasticity imaging of vascular tissues in a liquid environment by a scanning haptic microscope. *Journal of Artificial Organs*, **13**, 121–125.
21. Moriwaki, T., Oie, T., Takamizawa, K., Murayama, Y., Fukuda, T., Omata, S., Kanda, K., and Nakayama, Y., 2011, Variations in local elastic modulus along the length of the aorta as observed by use of a scanning haptic microscope (SHM). *Journal of Artificial Organs*, **14**, 276–283.
22. Egorov, V., Tsyuryupa, S., Kanilo, S., and Sarvazyan, A., 2008, Soft tissue elastometer. *Medical Engineering & Physics*, **30**, 206–212.
23. Gladwell, G.M.L., and Kleesattel, C., 1968, The contact –impedance meter-2. *Ultrasonics*, **6**, 244–251.
24. Kleesattel, C., and Gladwell, G.M.L., 1969, The contact –impedance meter-3. *Ultrasonics*, **7**, 57–62.
25. Kleesattel, C., 1970, Contact impedance meter. *Part IV. Ultrasonics*, **8**, 39–48.
26. Christiansen, D.L., Huang, E.K., and Silver, F.H., 2000, Assembly of type I collagen: Fusion of fibril subunits and the influence of fibril diameter on mechanical properties. *Matrix Biology*, **19**, 409–420.
27. Yamamura, N., Sudo, R., Ikeda, M., and Tanishita, K., 2007, Effects of the mechanical properties of collagen gel on the *in vitro* formation of microvessel networks by endothelial cells. *Tissue Engineering*, **13**, 1443–1453.
28. Ng, K., Hildreth, C.M., Phillips, J.K., and Avolio, A.P., 2011, Aortic stiffness is associated with vascular calcification and remodeling in a chronic kidney disease rat model. *American Journal of Physiology Renal Physiology*, **300**, 1431–1436.
29. Conde, M.V., Gonzales, M.C., Quintana-Vilamandos, B., Abderrahim, F., Briones, A.M., Condezo-Hoyos, L., Regadera, J., Susin, C., Gomez de Diego, J.J., Delgado-Baeza, E., Diaz-Gil, J.J., and Arribas, S.M., 2011, Liver growth factor treatment restores cell-extracellular matrix balance in resistance arteries and improves left ventricular hypertrophy in SHR. *American Journal of Physiology Heart and Circulatory Physiology*, **301**, 1153–1165.
30. Debrah, D.O., Debrah, J.E., Haney, J.L., McGuane, J.T., Sacks, M.S., Conrad, K.P., and Shroff, S.G., 2011, Relaxin regulates vascular wall remodeling and passive mechanical properties in mice. *Journal of Applied Physiology*, **111**, 260–271.
31. Tran, L.T., Park, H.J., and Kim, H.D., 2012, Is the carotid intima-media thickness really a good surrogate marker of atherosclerosis? *Journal of Atherosclerosis and Thrombosis*, **19**, 680–690.
32. Gosline, J., Lillie, M., Carrington, E., Guerette, P., Ortlepp, C., and Savage, K., 2002, Elastic proteins: Biological roles and mechanical properties. *Philosophical Transactions of the Royal Society B*, **357**, 121–132.

Implantation study of small-caliber "biotube" vascular grafts in a rat model

Masashi Yamanami, Hatsue Ishibashi-Ueda, Akihide Yamamoto, Hidehiro Iida, Taiji Watanabe, Keiichi Kanda, Hitoshi Yaku, et al.

Journal of Artificial Organs
The Official Journal of the Japanese Society for Artificial Organs

ISSN 1434-7229
Volume 16
Number 1

J Artif Organs (2013) 16:59-65
DOI 10.1007/s10047-012-0676-y

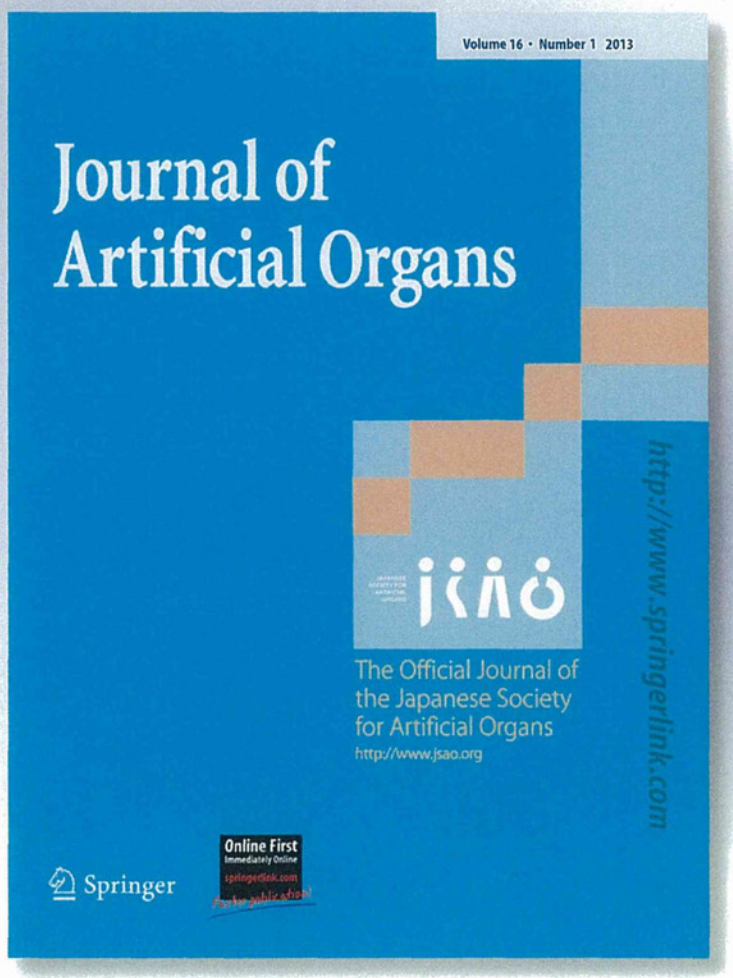

Springer

J Artif Organs (2013) 16:59–65
DOI 10.1007/s10047-012-0676-y

ORIGINAL ARTICLE

Implantation study of small-caliber "biotube" vascular grafts in a rat model

Masashi Yamanami · Hatsue Ishibashi-Ueda · Akihide Yamamoto · Hidehiro Iida · Taiji Watanabe · Keiichi Kanda · Hitoshi Yaku · Yasuhide Nakayama

Received: 7 July 2012 / Accepted: 9 November 2012 / Published online: 29 November 2012

Abstract We developed autologous vascular grafts, called "biotubes," by simple and safe in-body tissue architecture technology, which is a practical concept of regenerative medicine, without using special sterile conditions or complicated in vitro cell treatment processes. In this study, biotubes of extremely small caliber were first auto-implanted to rat abdominal aortas. Biotubes were prepared by placing silicone rods (outer diameter 1.5 mm, length 30 mm) used as a mold into dorsal subcutaneous pouches in rats for 4 weeks. After argatroban coating, the obtained biotubes were auto-implanted to abdominal aortas ($n = 6$) by end-to-end anastomosis using a custom-designed sutureless vascular connecting system under microscopic guidance. Graft status was evaluated by contrast-free time-of-flight magnetic resonance angiography (TOF-MRA). All grafts were harvested at 12 weeks after implantation. The patency rate was 66.7 % (4/6). MRA showed little stenosis and no aneurysmal dilation in all biotubes. The original biotube had wall thickness of about 56.2 ± 26.5 μm at the middle portion and mainly random and sparse collagen fibers and fibroblasts. After implantation, the wall thickness was 235.8 ± 24.8 μm. In addition, native-like vascular structure was regenerated, which included (1) a completely endothelialized luminal surface, (2) a mesh-like elastin fiber network, and (3) regular circumferential orientation of collagen fibers and α-SMA positive cells. Biotubes could be used as small-caliber vascular prostheses that greatly facilitate the healing process and exhibit excellent biocompatibility in vascular regenerative medicine.

Keywords Biotube · Vascular grafts · Autologous tissue · In vivo tissue engineering · Connective tissue

M. Yamanami (✉) · T. Watanabe · Y. Nakayama (✉)
Division of Medical Engineering and Materials, National Cerebral and Cardiovascular Center Research Institute, 5-7-1 Fujishiro-dai, Suita, Osaka 565-8565, Japan
e-mail: yamanami@koto.kpu-m.ac.jp

Y. Nakayama
e-mail: nakayama.yasuhide.ri@mail.ncvc.go.jp

M. Yamanami · T. Watanabe · K. Kanda · H. Yaku
Department of Cardiovascular Surgery, Kyoto Prefectural University of Medicine, Kyoto, Japan

H. Ishibashi-Ueda
Department of Pathology, National Cerebral and Cardiovascular Center, Osaka, Japan

A. Yamamoto · H. Iida
Department of Biomedical Imaging, National Cerebral and Cardiovascular Center Research Institute, Osaka, Japan

A. Yamamoto · H. Iida
Department of Medical Physics and Engineering, Division of Health Sciences, Graduate School of Medicine, Osaka University, Osaka, Japan

Introduction

Small-caliber arterial substitutes are needed for cardiac and peripheral revascularization procedures. For such small artery bypass grafting procedures, autologous arterial (e.g., internal thoracic artery and radial artery) or venous (e.g., saphenous vein) grafts are still the ideal vascular substitute [1–3]. However, many patients do not have a vessel suitable for use owing to the poor quality, inadequate size or length, or previous harvesting of such vessels [4]. Moreover, a second surgical procedure is required in order to obtain the necessary vessel initially. Small-caliber arterial substitutes have generally proved

inadequate largely because of the formation of thromboses and intimal hyperplasia [5, 6].

We developed autologous prosthetic tissues using "in-body tissue architecture" technology, which is a novel and practical approach of regenerative medicine based on the tissue-encapsulation phenomenon of foreign materials in living bodies [7]. This technology has the following advantages. The tissue prostheses can be fabricated in a wide range of shapes and sizes to suit the need of individual recipients, and most importantly, these prostheses do not require complex in vitro cell management procedures or exceptionally clean laboratory facilities, which are expensive and time consuming. This technology has been used for the development of cardiovascular tissues such as vascular grafts, namely biotubes [7–11], or heart valves, namely biovalves [12, 13]. Previously, the biotubes with 3-mm diameter were implanted into rabbit carotid arteries [10]. A high patency rate (9/11) was obtained at 12 weeks with endothelialization, dense collagen fibers with regular circumferential orientation, and a few elastin fibers. No aneurysm formation, rupturing, or stenosis was observed for up to 26 months without significant neointimal thickening [11].

In this study, further small-caliber biotubes with an inner diameter of 1.5 mm were auto-implanted to rat abdominal aortas for 12 weeks, and histological changes of biotubes after implantation were evaluated.

Materials and methods

Preparation of biotubes

A total of six adult female Wistar rats (age 8 weeks, weight 238.8 ± 58.6 g) were used in this experiment. All animals received care according to the Principles of Laboratory Animal Care (formulated by the National Institutes of Health, publication no.56-23, received 1985), and the research protocol (no. 9044) was approved by the ethics committee of the National Cerebral and Cardiovascular Center.

A silicone rod (diameter, 1.5 mm; length, 30 mm; Tigers Polymer, Osaka, Japan) was used as a mold. The rats were anesthetized with 1.5 % isoflurane (v/v air). A small incision was made in the shaved dorsal skin, and three molds were placed in dorsal subcutaneous pouches of each animal. After 4 weeks, the rats were anesthetized with 1.5 % isoflurane, and the implants were harvested. The three biotubes (internal diameter 1.5 mm) per one rat were obtained from the implants after trimming the peripheral tissues and pulling out the rods. One of the biotubes was used for autologous transplantation, and the others were used for measurement of burst strength or histological evaluation.

Measurement of burst strength

Biotubes ($n = 6$) and native abdominal aortas ($n = 6$) were used as samples. The native abdominal aortas were obtained at sacrificing for the implanted biotubes. One end of the biotubes was closed by tying with 4-0 silk threads and held at fixed distance to restrict the longitudinal distension and elongation. To the other end, a stainless-steel tube of 1.5 mm in external diameter was fixed with 4-0 silk threads to act as a cannula. Saline solution was pumped into the luminal cavities of the biotubes through the stainless steel tube at a rate of 50 mmHg/s until the biotubes ruptured. The burst strength was denoted by the water pressure at the instant of tube rupture, as measured by a pressure transducer (N5901; Nihon Denki Sanei, Inc., Tokyo, Japan).

Implantation of biotubes

Biotubes (length 20 mm; $n = 6$) were implanted to the infrarenal abdominal aorta using "the sutureless vascular connecting system" under microscopic guidance, similar to our previously reported system [14]. The connecting system consists of an introducing sheath and a connecting device. The introducing sheath was prepared by remodeling the catheter tubing (polyurethane of the 16G BD Insyte^{TM}, Becton, Dickinson and Company, NJ, USA). The connecting devices were custom-designed from the catheter (polyurethane, 16G BD Insyte^{TM}, Becton, Dickinson and Co., Franklin Lakes, NJ, USA). The dimensions of the devices were: 1.5 mm in length, 1.7 mm in external diameter, and 1.3 mm in internal diameter. In the wall of the catheter, circular micropores were processed by a CAD-assisted YAG laser ablation technique. Pore diameter was 400 μm, pore-to-pore distance was 500 μm, and the pore area to the entire area was 60 %.

Biotubes were treated by coating with argatroban (1 mg/cm^2; Mitsubishi Chemical Co., Tokyo, Japan) for 10 min in order to make it antithrombogenic immediately before implantation. The connecting devices were inserted into the proximal and distal ends of the rat aorta through the introducing sheath. Subsequently, the treated aortic ends were inserted into biotubes, followed by banding from the outside of the biotubes with 7-0 silk threads (Alfresa, Osaka, Japan). Patency was examined at the time of surgery by direct inspection. The wound was closed with 4-0 nylon sutures. Thereafter, the rats had free access to standard food and water. No anticoagulants or antiplatelet agents were administered postoperatively. After 12 weeks of implantation all biotubes were harvested.

Evaluation of graft status

Graft status was evaluated at 6 and 12 weeks after transplantation by 3-T contrast-free time-of-flight magnetic resonance angiography (TOF-MRA) under anesthesia induced by an intramuscular injection of pentobarbital (40 mg/kg). A human whole-body 3-T magnetic resonance imaging (MRI) scanner (Sigma, GE Healthcare, Milwaukee, WI, USA) was employed. The gradient coil system was capable of providing a maximum gradient amplitude of 40 mT/m. All sequence programs employed in this study were designed for clinical studies. A developed single-turn surface coil of 62 mm diameter was used for MR imaging. Contrast-free TOF-MRA was performed using a three-dimensional flow-compensated fast spoiled gradient recalled (3D-FSPGR) sequence [repetition time (TR) = 21 ms, echo time (TE) = 5.4 ms (out of phase), flip angle (FA) = 15°, slice thickness = 0.4 mm, field of view (FOV) = 80 mm × 60 mm, matrix = 288 × 192, locs per slab = 128, the number of excitations (NEX) = 1, scanning time = 5 min 58 s]. For suppressing venous signals, a region of 40 mm thickness on the caudal side of the measured slab was saturated. MR angiograms were analyzed by generating the partial maximum intensity projection (pMIP) with a commercial software package (AZE, Tokyo, Japan).

Histological examination

The specimens of the implanted biotubes were fixed with 10 % formalin, embedded in paraffin, sliced into short axis cross sections, and finally stained with hematoxylin-eosin, Masson's trichrome, Elastica van Gieson, or Siriusu red. Immunohistochemistry was performed using monoclonal antibodies against α-smooth muscle actin (anti-human α-SMA mouse monoclonal antibody clone 1A4; Dako Japan, Kyoto, Japan; 1:100 dilution) and factor VIII (anti-human von Willebrand factor mouse monoclonal antibody clone F8/86; Dako Japan, Kyoto, Japan; 1:100 dilution).

Results

Preparation of biotubes

After the molds (Fig. 1a) were inserted into the dorsal subcutaneous pouches of rats for 4 weeks, all molds were completely encapsulated with very thin homogeneous autologous connective tissues (Fig. 1b). Biotubes were obtained by removing the molds from capsule tissues (Fig. 1c). The efficiency of the biotube preparation was 100 %. The burst pressure of biotubes was 1085 ± 525 mmHg (mean ± SD), which is approximately half of that of rat aorta (2478 ± 628 mmHg).

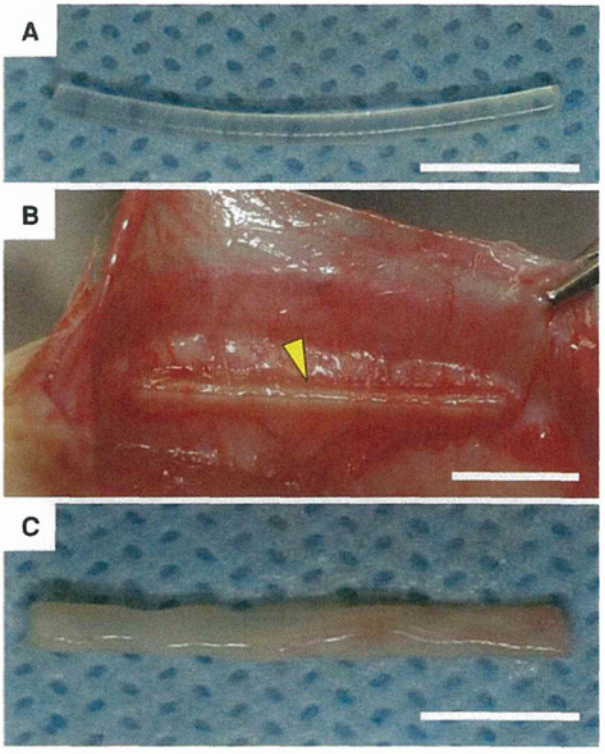

Fig. 1 **a** Silicone rods (diameter 1.5 mm, length 15 mm) were used as the molds. **b** The molds were embedded into dorsal subcutaneous pouches of rats for 4 weeks. The molds were completely encapsulated with connective tissues. **c** The obtained biotubes with thin wall (thickness 56.2 ± 26.5 μm). *Scale bar* 1.0 mm

Biotube implantation

Biotubes could be implanted easily into the rats using a custom-designed sutureless vascular connecting system, where no suturing treatment for anastomosis was needed (Fig. 2a). Total ischemia time for implantation was very short (34.8 ± 12.1 min). No bleeding was observed after declamping (Fig. 2b).

MRA distinctly visualized the patent graft connected to the abdominal aorta together with renal arteries and common iliac arteries (Fig. 3). However, pseudostenosis by artifact of the connection was observed in both anastomosis regions (arrows in Fig. 3). In the midgraft region, little stenosis and no aneurysmal dilation were observed in all patent grafts. The overall patency rate was 66.7 % (4/6). Two of the six grafts were occluded by thrombosis at 6 weeks after implantation.

Implanted biotubes were easily harvested with no damage because there were few adhesions between biotubes and surrounding tissues (Fig. 2c). In the obtained biotubes 12 weeks after implantation, macroscopic observation revealed an extremely flat surface including the region of connecting device, which was completely

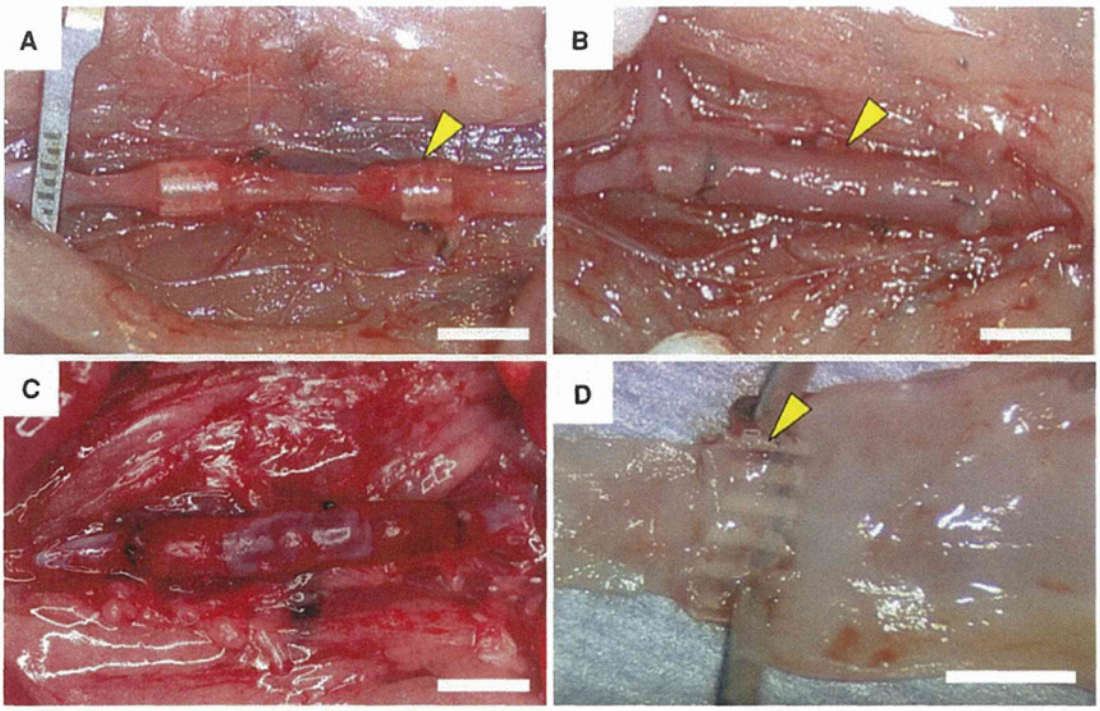

Fig. 2 **a** Insertion of two connecting devices, fabricated from catheter tubing (polyurethane of the 16G BD InsyteTM, Becton, Dickinson and Company, Franklin Lakes, NJ, USA), into the proximal and distal ends of the rat abdominal aorta through the introducing sheath under clamping. **b** The treated aortic ends were inserted into the biotube vascular graft, followed by banding from the outside of the biotube with 7-0 silk threads. Pulsation of the biotubes was noted immediately after declamping. **c** After 12 weeks of implantation, the biotube had little adhesion with surrounding tissues. **d** Macroscopic observation revealed an extremely flat luminal surface including the luminal regions of the connecting devices, which were completely impregnated into the vascular tissues (*scale bar* 3 mm)

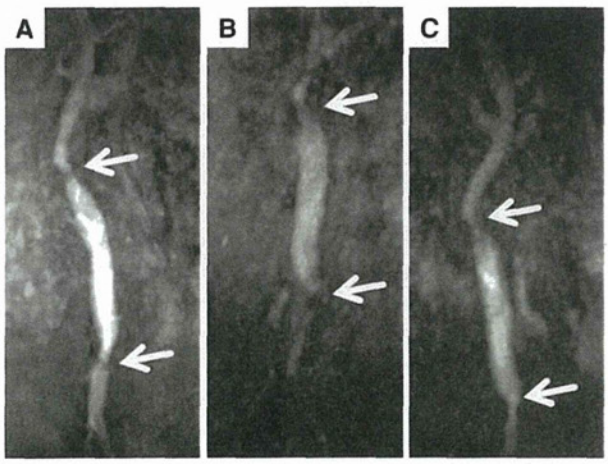

Fig. 3 MRA images of the rat abdominal aorta at 1 (**a**), 6 (**b**) and 12 (**c**) weeks after implantation of biotubes. Upper side of all photos indicates the proximal side. *White arrows* indicate the proximal and distal anastomosis regions of the abdominal aorta. A mechanical stenotic lesion, which may have been due to the anastomosis, was observed in both anastomosis regions. In the midgraft region, neither significant stenosis nor aneurysmal dilation was observed

impregnated into the developed thin tissues (Fig. 2d). In the circumferential cross section of midgraft region, the wall had grown thick, keeping the area of the lumen. Before implantation, wall thickness of the biotubes was 56.2 ± 26.5 μm (Fig. 4a-1). At 12 weeks after implantation, neointima was formed with wall thickness of 235.8 ± 24.8 μm (Fig. 4b-1).

Histological change

Before implantation biotubes were composed of collagen-rich tissue with no elastic fibers (Fig. 4a-2, a-3) and collagen fibers were randomly attached (Fig. 4a-6). No abnormal collection or infiltration of inflammatory cells was observed. The main cell component was fibroblasts with no vascular constituent tissues (Fig. 4a-4, a-5).

On the other hand, after 12 weeks of implantation the neointima was segregated in two layers, where the luminal layer with a mesh-like elastin fiber network (Fig. 4b-3) and circumferential oriented collagen fiber (Fig. 4b-2, b-6) were formed on the almost cell-free dense collagen basement

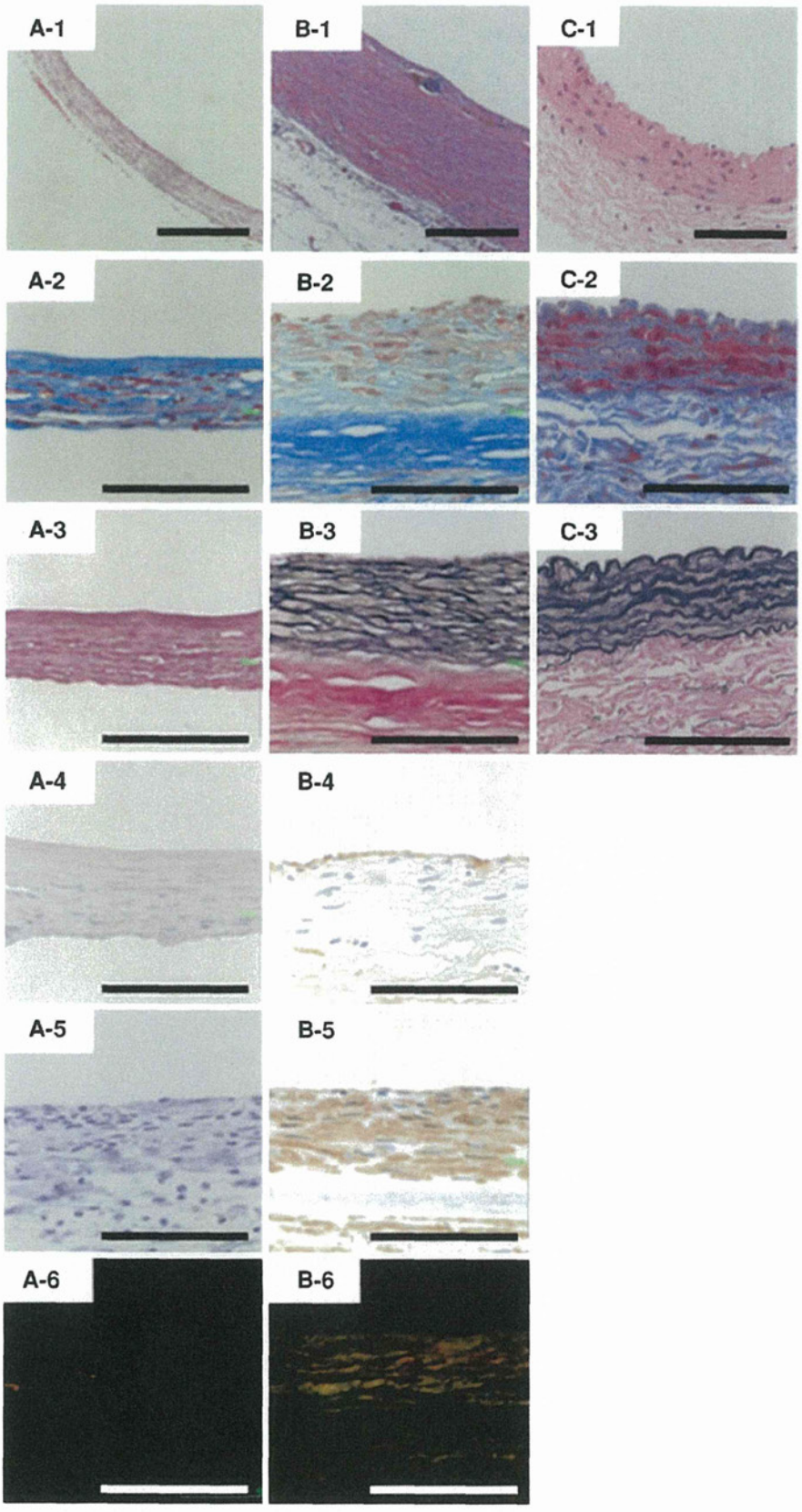

Fig. 4 The circumferential cross section of the biotube before implantation (**a-1–6**) and obtained at 12 weeks after implantation (**b-1–6**). The circumferential cross section of native rat abdominal aorta (**c-1–3**). Stained with H&E (**a-1**, **b-1**, **c-1**), Masson trichrome (**a-2**, **b-2**, **c-2**), Elastica van Giesson (**a-3**, **b-3**, **c-3**), factor VIII (**a-4**, **b-4**), α-SMA (**a-5**, **b-5**), and Sirius red (**a-6**, **b-6**). Masson trichrome stain revealed that it was composed of collagen-rich tissue. Polarizing microscopic observation after Sirius red stain showed circumferential orientation of the collagen fiber after implantation (**b-6**). Elastica van Giesson staining revealed an elastic fiber network in the neointima of the biotube after implantation (**b-3**). Immunohistological staining for factor VIII and α-smooth muscle actin revealed α-smooth muscle actin-positive cells (**b-5**) and endothelial lining at the luminal surfaces (**b-4**) of biotube after implantation (*scale bar* 100 μm)

layer. The construction of collagen and elastin fibers was very similar to that of native rat abdominal aorta (Fig. 4c-1, c-2). The luminal layer had many α-SMA-positive, myofibroblasts or smooth muscle cells (Fig. 4b-5) and was completely covered with endothelial cells (Fig. 4b-4).

Discussion

Tissue engineering combines the principles of engineering and biological sciences to develop viable structures that can replace diseased deficient natural structures. Some investigators have successfully implanted in vitro tissue-engineered vascular grafts in animals by using either decellularized natural tissues or biodegradable synthetic polymers as scaffolds [15–18]. However, these procedures require complicated cell-management protocols, including harvesting, seeding on appropriate scaffolds, and development of neotissues by culturing cells in bioreactors under strictly sterile conditions; all of these procedures are time consuming and expensive. On the other hand, in vivo tissue engineering can produce completely autologous tissues without any artificial support materials. Campbell et al. developed autologous vascular grafts in the abdominal cavities of rats or rabbits. Although the grafts had a relatively large internal diameter (3 mm) for small-caliber native aorta of rats, the high patency rate of 67 % was reported at 4 months of implantation by layering mesothelium cells on the luminal surface of myofibroblast-walled tubes [19].

In this study, we evaluated the potential of biotubes to generate a vascular graft for extremely small arteries (internal diameter 1.5 mm). The biotubes were implanted to the abdominal aorta of rats (internal diameter 1.3 mm) by end-to-end anastomosis using custom-designed sutureless connecting devices [15]. It must be verified whether biotubes can be sutured and have sufficient burst strength to withstand physiologic blood pressure or not. Because the biotubes have adequate mechanical properties for a vascular prosthesis, they were recently applied to carotid arteries [20] and abdominal aortas of beagle dogs [21]. In all implantations for systemic circulation, including those described in this study, neither rupture nor aneurysm formation was observed.

The patency rate of the biotubes at 12 weeks after implantation was high in this study (66.7 %). Because the main components of the original biotubes were collagen fibers and fibroblasts, it was considered that acellular luminal surfaces without endothelial cell coverage carry a substantial risk for thrombosis when exposed to the blood directly. In our previous implantation study of biotubes, all grafts without anti-thrombogenic coating were completely occluded at 2 weeks after implantation [10]. Strong anti-thrombogenicity, provided by the complete endothelialization of the luminal surfaces, is highly desirable. For this reason, most recent studies have focused on the creation of tissue-engineered cardiovascular implants using autologous endothelial cell seeding and bioreactor culturing prior to implantation. Seeding with autologous vascular cells on the luminal surface has provided a much higher patency rate than non-cell-seeded grafts [22]. However, such cell management and processing are complicated and invasive, and they will render the implants prone to infection. In this study, acute thrombus formation was considerably prevented by argatroban coating.

At 12 weeks after implantation, almost complete vascular tissue was re-constructed. Endothelial cells and SMCs migrated into the biotube and became organized into an endothelium and a media-like smooth muscle layer after implantation. In addition, mesh-like elastin network was formed on the basement dense collagen layer. Native-like vascular structure was regenerated in a short period of implantation. Therefore, the autologous connective tissue could serve as an ideal scaffold for vascular wall formation. Some investigators have discussed which cells and extracellular matrix remodeled tissue-engineered vascular grafts after implantation. Kuwabara et al. [23] suspected endothelial cells and smooth muscle cells were regenerated from circulating blood stem cells. Hibino et al. [24] reported neovessel formation arises from ingrowth of vascular cells from the neighboring blood vessel. Erman et al. described that endothelial coverage of the luminal surface, transmural cellular infiltration, and formation of neocapillaries in the graft body are the major graft healing characteristics [17]. In this study, it still remains unclear which cells and extracellular matrix remodeled biotubes after implantation. It is necessary to investigate this issue in the future.

Since the observation by MRA is simple and non-invasive, assessment of the status of small-caliber vascular grafts could be performed in the same rat at different times. The repeatable MRA observation in a single rat enabled correct assessment of the graft status over the follow-up period. Such repeatability will reduce the variation in results stemming from individual differences in experimental animals [25]. By using the connecting system, aortic clump time was only 30 min, which is about half that in the traditional suturing method [14]. Since no bleeding at the connecting parts occurred, hemostasis was very easy in all implantations. In addition, although pseudostenosis by artifacts of the connecting devices was observed at both anastomosis regions, there was no actual stenosis. The stenosis by suturing could lead to serious occlusion in small-caliber grafts. The control of the bleeding and minimal anastomotic stenosis using the connecting system induced reproductive results in the implantation study